Thermophoresis of DNA determined by microfluidic fluorescence

S. Duhr, S. Arduini, and D. Braun[a]

Dissipative Biosystems Lab, Applied Physics, Ludwig Maximilians Universität München, Amalienstr. 54, 80799 München, Germany

Abstract. We describe a microfluidic all-optical technique to measure the thermophoresis of molecules. Within micrometer-thick chambers, we heat aqueous solutions with a micrometer-sized focus of infrared light. The temperature increase of about 1 K is monitored with temperature-sensitive fluorescent dyes. We test the approach in measuring the thermophoresis of DNA. We image the concentration of DNA in a second fluorescence-color channel. DNA is depleted away from the heated spot. The profile of depletion is fitted by the thermophoretic theory to reveal the Soret coefficient. We evaluate the method with numerical 3D calculations of temperature profiles, drift, convection and thermophoretic depletion using finite element methods. The approach opens new ways to monitor thermophoresis at the single molecule level, near boundaries and in complex mixtures. The flexible microfluidic setting is a good step towards microfluidic applications of thermophoresis in biotechnology.

PACS. 87.23.-n Ecology and evolution – 82.70.Dd Colloids – 82.60.Lf Thermodynamics of solutions

1 Thermophoresis of biomolecules

Separation techniques such as gel electrophoresis are at core of modern DNA and protein biotechnology. However, electrophoresis is hard to miniaturize due to electrochemical effects at the metal-buffer interface and the tedious preparation of gel phases. We follow a new approach by driving biomolecules with strong but microscopic temperature gradients. Although the basic effect of this movement —called thermophoresis or Soret effect [1–5]— is now known for almost 150 years, the effect was only recently applied by us to DNA [6]. Our aim is to elucidate novel approaches to make use of thermophoretic driving forces in miniaturized biotechnology devices. Thermophoresis has an interesting history in applied chemistry and physics. For example, Clusius in 1938 found that convection can couple to thermophoresis in a way that highly amplifies the accumulation effect [7, 8]. The approach, called Clusius separation tube (Trennrohr) or gravitational column, is still used to measure thermophoretic constants of highly diffusive components. On the other hand, non-aqueous polymers were separated by thermal field flow (TFF) separation [9]. Recently, a miniaturized design was made by the group of Frazier with chamber dimensions as low as $2 \times 40 \times 0.03$ mm. It was used to separate beads in water [10,11]. In a recent speculation, we argued that thermophoresis could have played a role in molecular evolution near hydrothermal

vents [12]. Here we will discuss novel all-optical approaches in thin microfluidics to measure and apply thermophoresis for biomolecules in tiny volumes. We used the aforementioned approach to estimate thermal diffusion coefficients of DNA [6]. Working at the boundary between disciplines, we use fluorescence microscopy from biology, infrared heating from applied optics and complex liquid handling from microfluidics. Our approach can apply very strong temperature gradients ($> 1\,\mathrm{K}/\mu\mathrm{m} = 10000\,\mathrm{K/cm}$) in flexible microfluidic settings under excellent fluorescence microscopy conditions. We detect both temperature and particle concentration by fluorescence. This yields a flexible experimental platform to confirm basic characteristics of thermophoresis. Microscopic imaging allows to measure slowly diffusing molecules within reasonable times. For example, 50.000 base pair λ-DNA (diffusion constant of $D = 10^{-12}\,\mathrm{m}^2\,\mathrm{s}^{-1}$) can be measured within 300 s. Since we microscopically image the sample, artefacts such as dirt or sample inhomogeneity are immediately recognized. Also liquid movement such as convection or drift yields precise fingerprints in the concentration image. Moreover, with the fluorescence approach, we have the prospect of following thermophoresis down to the single molecule level. We are not only motivated by possible applications of thermophoresis. To our day, the theoretical description of thermophoresis in liquids is not yet understood. The out-of-equilibrium nature of thermophoresis makes its description difficult to be described. The recent work of many labs and researchers, for example of Werner

---

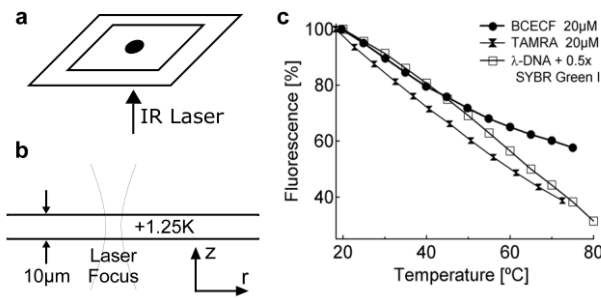[a] e-mail: `dieter.braun@physik.lmu.de`, `mail@dieterb.de`

Fig. 1. Temperature control for all-optical imaging of thermophoresis. (a) A thin chamber is sandwiched between glass cover slides. The center of the chamber is locally heated by a a moderately focussed infrared laser. (b) We choose a chamber thickness of $10\,\mu$m and heat moderately in the center by 1.25 K. (c) The local temperature is inferred from the temperature dependence of pH-dependent fluorescent dyes in TRIS buffer as measured independently in a fluorometer. The negative slopes mean that a darkening in the fluorescent image can be interpreted as increase in temperature.

Köhler [13,14] and Roberto Piazza [15–17] shed new light into the mechanics of thermophoresis of polymers, micelles and proteins in aqueous solutions. Only by collecting thermophoresis data in as diverse as possible situations we can hope to understand the effect.

2 Materials and method

2.1 Chamber

For a most simple measurement approach, we enclose $2\,\mu$l of sample between 0.17 mm thick cover slips (Roth Laborbedarf). The sample is placed on a 24×40 mm cover slip and closed by pressing a smaller $18\,\text{mm} \times 18\,\text{mm}$ cover slip from the top. The liquid stops at the boundary of the smaller cover slip and wets its area. Then it is sealed with immersion oil at the periphery (Fig. 1a). Based on the volume-area ratio, we expect a sample film of $6\,\mu$m thickness. However, since the immersion oil creeps into the chamber from the sides, the chamber might be 1–$2\,\mu$m thicker. It should be noted that the method does not sensitively depend on the precise knowledge of the chamber thickness. After 20 minutes of equilibration, drifts in the chamber drop typically below $0.03\,\mu$m/s.

2.2 Microfluidics

For more sophisticated geometries, we use the well-known PDMS-SU-8 microfluidics. The low IR-absorption and low thermal conductivity ($\lambda = 0.18\,\text{W}\,\text{m}^{-1}\,\text{K}^{-1}$) makes PDMS a perfect material for infrared heating. The connection between PDMS microfluidics and the glass needs however special care to be reliable and non-leaking. We use PDMS-PDMS bonding, but change the protocol of

Quake's group [18] to keep the chamber compatible with oil objectives. The process is as follows. A thin layer of $1:5$ PDMS is spin coated on 24×40 mm cover slips at 2000 rpm, leading to a film of about 20–$30\,\mu$m as measured by weighing the slides. After curing for 15 min on a $70\,^{\circ}$C hot plate, the PDMS is solid but still sticky to glue upon contact to the $1:10$ bulk PDMS. The channels seal fully after curing at $60\,^{\circ}$C for 2 h.

2.3 Infrared heating (Fig. 1a,b)

The fiber-coupled solid-state laser Furukawa FOL1405-RTV-317 yields a center wavelength of $\lambda = 1480$ nm at 320 mW maximum power. It is mounted on an ILX Lightwave LDM-4984 and current and cooling controlled by an ILX Lightwave LDC-3744B. The current can be modulated from the analog output of a computer-controlled digital-analog DAQPAD-6070E Firewire-based I/O-card from National Instruments using LabView 7.0. The infrared light is coupled out of the fiber to a $1/e^2$ diameter of 3 mm with a Thorlabs output coupler F260FC-C and then scanned by a Cambridge Technology 6200-XY Scanner with Driver 67120. After fully expanding the beam to 6 mm by a $19\,\text{mm}/40\,\text{mm}$ focal distance beam expander (Thorlabs), it is focussed with a infrared corrected Mitutoyo objective NIR $5\times$ with working distance 38 mm and numerical aperture 0.14. We achieve a minimal Gaussian $1/e$ profile width of $8\,\mu$m (Fig. 1b). The focus can be easily broadened by moving the thin chamber along the optical axis in z-direction. Water highly absorbs at this wavelength with an attenuation length of $k = 400\,\mu$m.

2.4 Fluorescence imaging of temperature (Fig. 1c)

We exploit the pH drift of 10 mM TRIS buffer upon temperature change. The drift is measured by a pH-sensitive fluorescent probe. This allows usage of highly soluble fluorescent probes. All optical probes of temperature pursued previously only worked for non-aqueous solutions. The temperature dependence of the dye was measured with a temperature-controlled fluorometer (Fig. 1c). Near $20\,^{\circ}$C, we obtain temperature sensitivities of $B = -1.13\%/\text{K}$ for TAMRA ($20\,\mu$M, C-300, molecular probes), $B = -0.95\%/\text{K}$ for BCECF ($20\,\mu$M, B-1151 mixed isomers, molecular probes).

2.5 DNA and DNA staining

We use the DNA of the bacteria-attacking virus lambda (λ). λ-DNA has a length of 48502 base pairs. We stain DNA with low concentrations of SYBR Green I (S-7563, molecular probes). Starting from $0.46\,\mu$g/μl (14 nM) stock solution (Invitrogen/Gibco BRL, Cat. No. 25250-010), we dilute the DNA $1:10$ into a 10 mM TRIS-HCl buffer (pH 7.8). Short DNA with a length of 27 base pairs was hybridized from synthetically produced oligomers

(IDTDNA) and diluted to $10\,\mu$M. We add $2\times$ SYBR-Green and $20\,\mu$M of TAMRA. The dye intercalates into DNA, but changes the overall DNA characteristics only minimally. For example, SYBR-stained DNA can still be replicated with a PCR reaction.

2.6 Fluorescence imaging and bleaching correction

We use the microscope Zeiss Axiotech Vario with objective Plan Fluar $40\times$, NA 1.3 oil. For illumination, a Luxeon High power LEDs LXHL-LX5C was built into a standard halogen lamp housing and driven at 30–700 mA by an ILX Lightwave LD-3565 current source. Fluorescence filters were from AHF-Analysentechnik, Tübingen for FITC (HQ F41-001). Detection was provided with a 12-bit camera PCO Sensicam QE 670KS with 65% quantum efficiency. The camera has a linear light response at negligible background levels. For slow diffusing specimen, the illumination was switched off during equilibration to reduce bleaching. Fluorescence imaging averages the fluorescence across chambers thinner than about $30\,\mu$m. This can be demonstrated by focussing a layer of adsorbed fluorescent beads. For objectives with low numerical aperture, averaging spans almost 1 mm as documented in [6]. However, we had to check that this averaging across the chamber is independent of lateral temperature gradients. These can bend the light rays of excitation and emission from their optimal configuration, leading to a defocussed image and lower fluorescence readings. Note that this lensing effect differs from thermal lensing methods which measure the focal length of the created lens in the far field. Since defocussing-induced fluorescence imaging artefacts are small at NA = 0.4 due to the large averaging focus, we can use it as reference. We compared fluorescence images of the same radial temperature profiles measured at NA = 0.4 and NA = 1.3. Both images differed only in the central $10\,\mu$m region relative to each other by 5%. We therefore infer that averaging fluorescence across thin chambers is reliable even under lateral temperature gradients used in our experiments. To be independent of inhomogeneous fluorescence illumination, images in the heated state are normalized against previously taken cool pictures. Also, a cool picture after measurement is taken to allow for a linear bleaching correction over time. In all experiments, illumination intensity is low such that bleaching was below 20% and linear bleaching correction was applicable.

3 Numerical simulations

3.1 3D simulation of temperature profile (Fig. 2)

We calculate the shape of the temperature profile across the chamber. Since the fluorescence measurements average all fluorescence across the chamber, its exact profile should not affect the result. The laser focus is described with a minimal $1/e^2$-radius of $\sigma_0 = 8\,\mu$m, attenuation length $k = 400\,\mu$m, refractive index of water $n = 1.333$ focussed
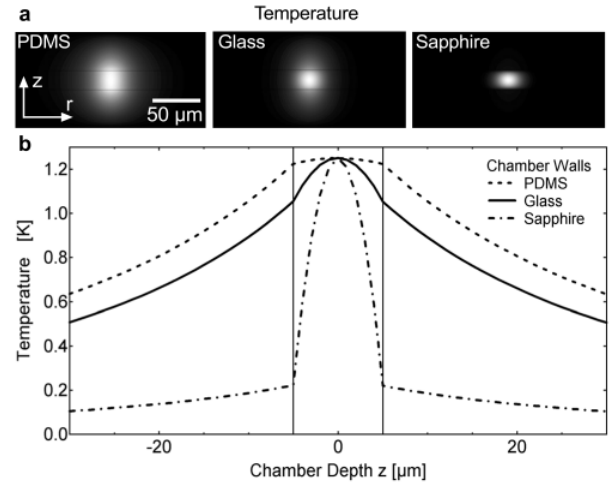

Fig. 2. Temperature profile in a $10\,\mu$m thin chamber (theory). (a) The recorded fluorescence images average across the thin chamber. The detailed temperature profile across the chamber was calculated for different chamber wall materials. (b) Whereas low thermal conductive PDMS leads to almost constant temperature profile across the z-axis, the increased thermal conductivity of glass or even sapphire yields steeper parabolic temperature profiles.

at height $z = z_0$ in the center of the chamber with a numerical aperture of NA = 0.14 with Gaussian shape in geometrical approximation. We obtain the absorbed light power density $I(r,z)$:

$$\sigma = \sigma_0 + \tan\left[\arcsin\left(\frac{NA}{n}\right)\right] \times |z - z_0|,$$

$$I(r,z) \propto \sigma^2 \times \exp\left(-\frac{2r^2}{\sigma^2}\right) \times \exp\left[-\frac{(z-z_0)}{k}\right]. \quad (1)$$

It should be noted that the chamber thickness below $10\,\mu$m is much smaller than the attenuation length of the light. Therefore, the focus can be approximated by

$$I \propto \exp\left(-\frac{2r^2}{\sigma^2}\right). \quad (2)$$

The total absorbed laser power is adjusted to increase the chamber liquid temperature in the center by 1.25 K above room temperature in all shown simulations. The light pressure pushes the liquid with a radiation force density f obtained from dividing the absorbed light intensity I by the light velocity c_0:

$$f = \frac{I}{c_0}. \quad (3)$$

All numerical calculations are done with the finite element simulator Comsol Femlab 2.3.154 + Chemical Engineering Module. The physical parameters of the materials were as follows. For water, density $\rho = 1000\,\text{kg}\,\text{m}^{-3}$, heat capacity $c = 4200\,\text{J}\,\text{kg}^{-1}\text{K}^{-1}$ and heat conductivity $\lambda = 0.54\,\text{W}\,\text{m}^{-1}\text{K}^{-1}$; for PDMS, $\rho = 1030\,\text{kg}\,\text{m}^{-3}$, $c = 1260\,\text{J}\,\text{kg}^{-1}\text{K}^{-1}$ and $\lambda = 0.18\,\text{W}\,\text{m}^{-1}\,\text{K}^{-1}$; for glass, $\rho =$

$2600 \, \mathrm{kg \, m^{-3}}$, $c = 780 \, \mathrm{J \, kg^{-1} K^{-1}}$ and $\lambda = 1.4 \, \mathrm{W \, m^{-1} K^{-1}}$ and for sapphire, $\rho = 3980 \, \mathrm{kg \, m^{-3}}$, $c = 750 \, \mathrm{J \, kg^{-1} K^{-1}}$ and $\lambda = 34 \, \mathrm{W \, m^{-1} K^{-1}}$. All FEMLab model files can be obtained from the authors. To show the influence of heat conductivity of the chamber on the temperature profile, we simulated the temperature in a $10 \, \mu \mathrm{m}$ thick water film between $170 \, \mu \mathrm{m}$ thick chamber walls. All calculations were done in cylinder coordinates and therefore reflect a full 3D model. The simulation of temperature across the chamber is seen in Figure 2. The liquid temperature is almost constant across the chamber for isolating PDMS chamber walls. It becomes parabolic with small tails for glass walls and is reduced for sapphire chamber to almost perfect parabolic shape. Profiles of the temperature across the chamber in the heating center are shown in Figure 2b. To reach the same temperature, the laser power has to be increased 4.7-fold as we go from PDMS to glass and again 4.7-fold as we change from glass to sapphire.

3.2 Theory of thermophoresis (Fig. 3)

Thermophoresis is described by a phenomenological term that extends Fick's first law. The concentration current density j depends on the concentration c given in the molar ratio of molecules *versus* liquid molecules as follows:

$$j = -D[\nabla c + S_T c(1 - c)\nabla T] \tag{4}$$

The Soret coefficient S_T is the ratio of the thermal diffusion coefficient D_T and the diffusion coefficient D: $S_T = D_T/D$. The description of thermophoresis by equation (4) is phenomenological and still lacks a microscopic understanding. Further measurements of thermal diffusion coefficients D_T are important to reveal the detailed mechanism underlying thermophoresis.

We use equation (4) to simulate thermophoresis in 3D by finite element methods in cylinder coordinates. The result is shown in Figure 3. The water in the chamber is heated to a peak temperature increase of 1.25 K (Fig. 3a). With the diffusion constant of λ-DNA [19] of about $D = 1 \times 10^{-12} \, \mathrm{m^2 \, s^{-1}}$ and the thermal diffusion coefficient $D_T = 0.4 \times 10^{-12} \, \mathrm{m^2 \, K^{-1} \, s^{-1}}$ that we measure later, we find the thermophoretic depletion of Figure 3b. The concentration of DNA in the center of the chamber drops to 60% with a spatial distribution directly governed by equation (5). It is derived for small probe concentrations c and constant D_T in non-moving liquids from equation (5):

$$\frac{c}{c_0} = e^{-S_T(T-T_0)} \approx 1 - S_T(T - T_0) . \tag{5}$$

For small temperatures $\Delta T D_T/D \ll 1$, the linear extension is valid and will be used heavily in the derivations of the following section in fluorescence imaging corrections.

Any central heating leads to thermal convection from lateral temperature gradients. The measurement idea is to choose a thin chamber to highly dampen convection. The convection is driven in the same direction both by thermal expansion of water under gravity and by light
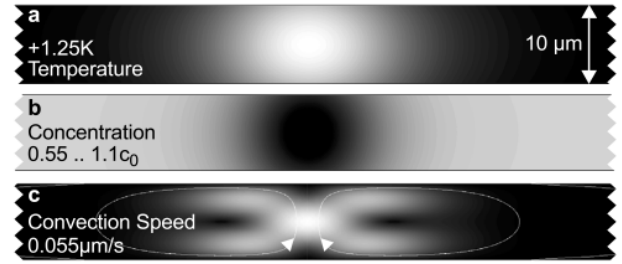

Fig. 3. Convection and thermophoresis in thin chamber (theory). Any central heating leads to thermal convection from lateral temperature gradients. The measurement idea is to choose a thin chamber to damp convection. The validity of the approach is tested by finite element solutions of the Navier-Stokes equation. We find a maximal convection speed of $0.055 \, \mu \mathrm{m/s}$. Even for slow-diffusing species such as λ-DNA ($D = 1 \times 10^{-12} \, \mathrm{m^2/s}$), convection is not fast enough to perturb the concentration profile.

pressure of the heating infrared light. We solve the Navier-Stokes equations for water together with heat transfer and the diffusion equation of DNA. The maximal convection speed is found to be $0.055 \, \mu \mathrm{m/s}$. This convection has the potential to perturb the concentration profile shaped by thermophoresis. However, even for slow-diffusing species such as λ-DNA, the simulation shows that convection is not fast enough to change the concentration profile. The concentration profile shows the same shape as the temperature profile and can be still directly inferred from non-flow conditions given by equation (5).

3.3 Temporal response and equilibration time (Fig. 4)

Under conditions of small temperature differences and low convection, we can reduce the description to a one-dimensional axial model. We add a linear cooling term to model the surface cooling of the chamber. It is adjusted to obtain the radial temperature profile of the 3D calculation. The reduction of the theoretical model to one dimension allows easy simulations of the temporal response in the experiment. The radial depletion of λ-DNA can already be seen after seconds and develops into a steady-state profile after several 100 s (Fig. 4a). We find a similar temporal response also in the experiments. The final depletion reflects the applied temperature increase of 1.25 K above room temperature according to equation (5). The temporal drop of the concentration of DNA in the center of the chamber is a non-trivial function of time due to the radial geometry of the measurement (Fig. 4b). The final central concentration drops to 60% of the initial concentration after more than 100 s.

3.4 Convection artefact in thicker chambers (Fig. 5)

Thicker chambers increase the speed of convection and can even turn thermophoretic depletion into accumulation [6]. We keep the heating of the chamber constant
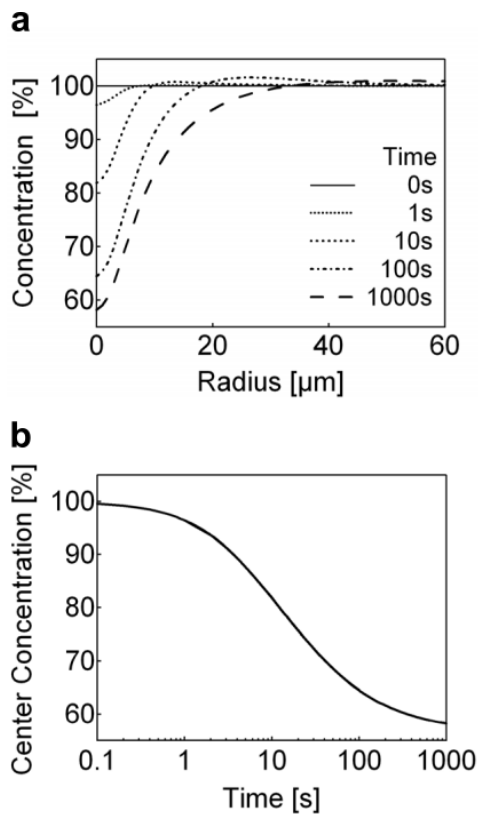
Fig. 4. Thermophoresis over time (theory). Under conditions of small temperature and low convection, we can reduce the description to an axial model with only one radial dimension. This allows for simulations of the temporal response of thermophoretic depletion. (a) The radial profile reaches steady state for λ-DNA after several 100 s. It reflects the applied temperature profile according to equation (5). (b) The concentration of DNA in the center of the chamber drops with a non-trivial characteristics due to the Gaussian radial heating geometry of the measurement. The final central concentration drops to 60% of the initial concentration after more than 100 s.

Fig. 5. From depletion to accumulation by convection in thicker chambers (theory). We keep the heating of the chamber constant at 1.25 K above ambient temperature and increase the chamber thickness. For a fast-diffusing 50 base pair DNA, this has no effect on the central depletion profile of about 98%. However, for slow-diffusing λ-DNA, chamber thickness even at these low temperatures is crucial. Already at $20\,\mu$m the concentration profile becomes asymmetric at reduced minimal concentration. For a $50\,\mu$m thick chamber, we find conditions of enhanced concentration ($c = 1.1c_0$) at the lower chamber wall. This accumulation to a point by thermophoresis was reported earlier in thicker chambers under stronger heating [6]. The convection artefact of thicker chambers is easily seen experimentally when a concentration profile does not match the theoretical profile that is calculated from the measured temperature.

to 1.25 K above ambient temperature and increase the chamber thickness. As we choose chamber thicknesses of 10, 20 and $50\,\mu$m, the maximal convection speed has values of 0.055, 0.22 and $1.5\,\mu$m/s. The flow characteristics is similar to Figure 3c. We show two scenarios: fast-diffusing DNA of length around 50 base pairs with $D = 34 \times 10^{-12}\,\mathrm{m^2\,s^{-1}}$ (Fig. 5, left) and slow-diffusing DNA with about 50.000 base pairs $D = 1 \times 10^{-12}\,\mathrm{m^2\,s^{-1}}$ (Fig. 5, right). For both we assume the same thermal diffusion coefficient $D_T = 0.4 \times 10^{-12}\,\mathrm{m^2\,K^{-1}\,s^{-1}}$. Faster convection has no effect on the depletion profile and we can measure thermophoresis using equations (4–10). We might even enhance the temperature to obtain better signals. For slow-diffusing DNA, chamber thickness even at low temperatures is crucial. Already at $20\,\mu$m chamber thickness, the concentration profile becomes asymmetric and the center concentration is reduced. For a $50\,\mu$m thick chamber, we even find a 10% enhancement of concentration ($c = 1.1c_0$) at the lower chamber wall. This accumulation by thermophoresis and convection was experimentally
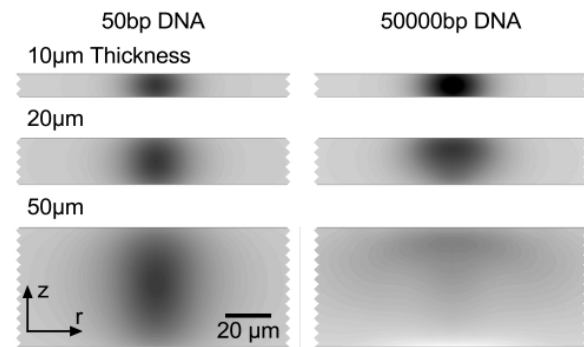
found by us before [6]. In thermophoretic measurements, this convection artefact of thicker chambers can be seen in a concentration profile which then does not match the measured temperature profile. Therefore, the condition of a too thick chamber can be readily detected. The plume of convective-thermophoretic accumulation is similar in shape to the standing-wave oscillations studied by Lücke *et al.* [20]. In both cases, concentration differences created by thermophoresis are transported by convection. However, the detailed mechanism is different since here the convection is only driven by thermal expansion.

3.5 Influence of light pressure on convection (Fig. 6)

The effect of light pressure upon absorption is not negligible. Convection in thin chambers differ when infrared heating is applied from top or from the bottom. The effect can be experimentally seen for example when we directly put the end of the glass fiber of the laser into water: a flow that is driven by the light coming out the fiber is clearly visible. This light pressure effect has to be taken into account also in thermophoresis measurements by thermal lensing as we indicated to the authors of [17], where an estimate of the effect and a discussion of its dependence on the experimental conditions is given. We show here that the effect of light pressure can reduce the upward convection. It is even possible to invert the convection. However, we cannot directly balance convection by light pressure as shown in the following. For the simulation, we choose a
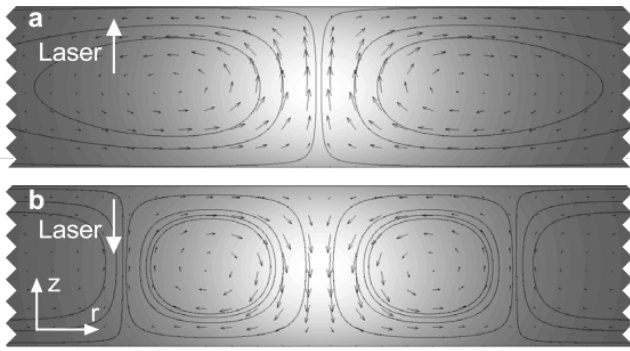
Fig. 6. Effect of light pressure on convection (theory). Momentum of light cannot be neglected when water is heated by infrared radiation. We give an example for a 50 μm thick chamber heated by 1.25 K in the center. Without light pressure, the maximal convection speed would be +0.15 μm/s. (a) If the light comes from below, the convection speed increases to 0.5 μm/s. (b) Light from above can invert the convection flow, forcing it down in the center with −0.2 μm/s. Only in the periphery it still convects upwards with +0.05 μm. Convection therefore is not balanced in detail, but reduced if IR-heating is applied from above.

50 μm thick chamber heated again to 1.25 K above ambient temperature in the center. Without light pressure, the maximal convection speed would be +0.15 μm/s. If the light comes from below, the convection speed increases to +0.5 μm/s (Fig. 6a). Light from above can invert the convection flow, forcing it down in the center with −0.2 μm/s. It convects only in the periphery upwards with +0.05 μm (Fig. 6b). These two counter-moving convection tubes are formed due to the different locations of force generation. Heat conduction broadens the temperature distribution as compared with the light radiation that heats and at the same time moves the liquid with its light pressure. Therefore, at the periphery, fluid flow is directed upwards since temperature is still increased, but light pressure from above is too low. In first order, the effect of convection reversal by light radiation is not depending on the chamber thickness. This is because the absorbed light radiation that pushes the liquid depends quadratically on the chamber thickness. The reason is that the system is dominated by the cooling walls and thus by quadratically scaling diffusion of heat diffusion to the walls. In a viscous laminar system, this is proportional to the speed of the liquid. Therefore, liquid flow from radiative pressure scales quadratically with the thickness of the chamber if the chamber is heated to the same temperature. On the other hand, thermal convection in a chamber heated to the same temperature scales quadratically with the chamber thickness as discussed in [17]. Therefore, both effects scale equally for thin chambers. However, in our full 3D simulations, the light pressure effect is decreasing more for thicker chambers. For example a 100 μm thick chamber yields a central downward flow of only −0.075 μm/s, yet heating with light from below gives an upward velocity of +2 μm/s.
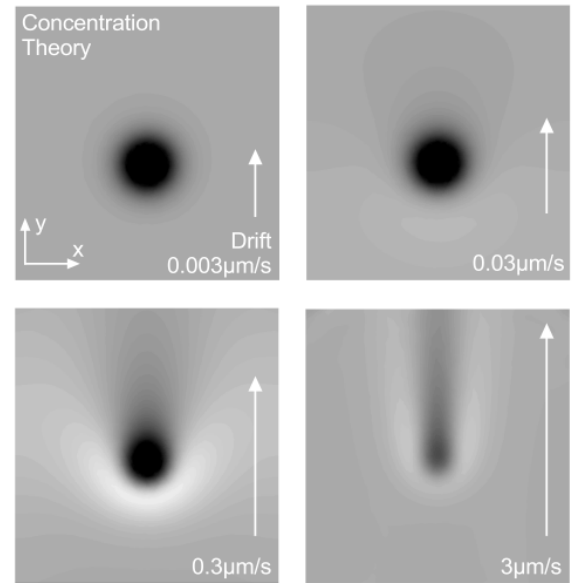

Fig. 7. Flow distortion by solution drift (theory). Besides convection, drift of the liquid in the chamber is a major source of artefact in a thermophoresis measurement. However, the imaging approach allows to detect this drift easily. We show 2D simulations of thermophoresis of λ-DNA for a liquid drift of 0.003, 0.03, 0.3 and 3 μm/s. The shown chamber section is 100 μm × 100 μm wide. The heating spot parameters are the same as in Figures 3–5. Already for drifts below 0.03 μm/s we see a noticeable distortion of the radial profile which increases as the drift velocity increases. At about 0.3 μm/s, a strong accumulation is found below the heating spot as thermophoretic drift and liquid drift counteract. Experimentally, drift-free chambers are prepared by sealing the chamber with oil and waiting 20 min to equilibrate.

3.6 Thermophoresis against horizontal drift (Fig. 7)

A small horizontal drift of the solution is commonly found under microfluidic conditions. Typically, it originates for example from external pressures, gravitational flow, evaporations at the openings of the chamber or simply from thermal expansion induced by inhomogeneous chamber temperatures. The drift distorts the depletion profile along the flow. Besides convection, drift of the liquid in the chamber is a major source of artefact in a thermophoresis measurement. The imaging approach allows to detect drift very easily from an asymmetric concentration image. This effect can be simulated when we extend the one-dimensional axial simulation used in Figure 4 to a 2D situation. We calculate the thermophoresis of λ-DNA for a central liquid drift of 0.003, 0.03, 0.3 and 3 μm/s. A 100 μm × 100 μm section of the chamber is shown in Figure 7. The heating parameters are identical to the ones used beforehand in Figures 3–5. For drifts below 0.03 μm/s we see a noticeable distortion of the radial profile which increases as the drift velocity increases. At about 0.3 μm/s, a strong accumulation is found in the region of the heating spot where thermophoretic drift and liquid drift have opposite direction. Here, thermophoretic drift and liquid

drift counteract. Experimentally, it is often a challenge to meet the drift-less criteria for slow-diffusing specimen. For chambers made out of cover slips, sealing the chambers with oil and waiting for 20 min yields drift-free chambers in most cases. The effect of drift can be much reduced by using dead end structures in microfluidic channels.

4 Fluorescence imaging of concentration and temperature

We will discuss in the following how concentration and temperature can be extracted from fluorescence images. As described in materials and methods, we measured fluorescence intensities F_T for the temperature dye and F_c for the DNA dye. Both are imaged in the cold state at T_0 —denoted by F_T^0, F_c^0— and later in the heated state at temperatures $T(x, y)$ —denoted by F_T, F_c. The temperature-sensitive dye depends on small temperature changes $T - T_0$ with a linear slope B given in percent fluorescence change per K temperature change [%/K] (Fig. 1c). The fluorescence intensity of the probe marker F_c reports the probe concentration c:

$$F_T = F_T^0[B(T - T_0) + 1] , \qquad F_c = F_c^0 \frac{c}{c_0} , \qquad (6)$$

F_c^0 is the fluorescence intensity of the probe marker at both background concentration c^0 and cold temperature T_0. Inserting equation (6) into the linearly approximated form of thermophoretic depletion given by equation (5) leads to a linear relationship between F_c and F_T:

$$\frac{F_c}{F_c^0} = 1 - \frac{S_T}{B} \frac{F_T - F_T^0}{F_T^0} . \qquad (7)$$

Both linear relationships, namely that of F_T to the temperature according to equation (6) and that of F_c to F_T according to equation (7) makes it possible to infer them from the images which inherently record a cross-chamber average. This means that averaging across the chamber, which we will denote by the operator $\langle \, \rangle$, leads to the same prefactor for both F_T and F_c since they integrate over the same functional shape. Thus, we can infer the Soret coefficient directly from the measured, averaged fluorescence intensities $\langle F_T \rangle$ and $\langle F_c \rangle$:

$$S_T = \frac{D_T}{D} = - \left(\frac{\langle F_c \rangle}{\langle F_c^0 \rangle} - 1 \right) \frac{\langle F_T^0 \rangle}{\langle F_T \rangle - \langle F_T^0 \rangle} B . \qquad (8)$$

To be more precise, we have to include into the description a possible temperature dependence of the probe marker itself. For example, SYBR-Green has a marked temperature dependence of $B^* = -0.96\%/$ K ($0.5\times$ SYBR Green I with λ-DNA, Fig. 1c). We include this effect with the following substitution of the concentration fluorescence from equation (6):

$$F_c = F_c^0 \frac{c}{c_0} [B^*(T - T_0) + 1] . \qquad (9)$$

The problem is that this additional temperature dependence breaks the linear averaging argument used above. Now, other than in equation (7), F_c is a non-linear function of the relative temperature change $f_T = (F_T - F_T^0)/F_T^0$:

$$\frac{F_c}{F_c^0} = -\frac{S_T}{B} \left[f_T + f_T^2 \frac{B^*}{B} \right] . \qquad (10)$$

We have to consider this non-linearity especially for strong heating and have to take into account the precise temperature characteristic across the chamber. However, for our experiments with λ-DNA, the relative temperature change f_T is only 1.4%. This is much larger than the quadratic term $f_T^2 B^*/B = 0.017\%$, leading to an error if we neglect the effect of 1.2% in S_T. This deviation is however below our overall measurement precision.

We have to consider another possible source of error. In using temperature-sensitive dyes with characteristics measured in thermodynamic equilibrium in a fluorometer, we assume that thermophoretic depletion of the temperature dye itself can be neglected. In a preliminary estimation, the dye has a similar monomer thermodiffusion as the highly charged DNA, namely approximately $D_T = 0.4 \times 10^{-12} \, \text{m}^2 \, \text{K}^{-1} \, \text{s}^{-1}$. Together with the diffusion constant of a similar dye FITC, $D = 5.1 \times 10^{-10} \, \text{m}^2 \, \text{s}^{-1}$, we infer a Soret coefficient $S_T = 0.0008 \, \text{K}^{-1}$. Preliminary measurements confirm similar Soret coefficients for the used temperature dye. We can infer the Soret coefficient of the dye from fast recordings of the temperature fluorescence upon laser heating. After a fast fluorescence drop we find a slower response which we attribute to thermophoretic depletion. The ratio of the two drops allow to infer the Soret coefficient of the dye, very similar to beam deflection methods of Giglio and Vendramini [21]. We can take for example a temperature increase of 1 K above room temperature. The intensity of the dye decreases by about 1% due to its temperature sensitivity. Its concentration due to thermophoresis is depleted however by only 0.08%. Thus, our measurement of temperature using fluorescent dyes is 8% too high. Hence, thermal diffusion coefficients have the possibility to be systematically too low by 8%. The effect of this systematic error will be studied in more detail in the future since it can be suppressed by taking the temperature image at an optimal time after switching on the laser.

5 Measuring thermophoresis of DNA

5.1 Recapitulation of method

Until now we have checked that thermophoresis should be measurable by microfluidic fluorescence without artefacts. An infrared focus is heating water optically to a temperature which we detect by fluorescence imaging. It causes a thermophoretic depletion that is recorded by fluorescence at a different color. By comparing the temperature profile with the concentration profile in steady state, we can infer the Soret coefficient.

We have checked that both the temperature profile and the concentration profile across the chamber have the same parabolic shape. Since we are in the linear regime of equation (5), the averaging across the chamber performed by fluorescence imaging introduces no artefact. By using a $< 10\,\mu m$ thin chamber, convection is too slow to introduce a detectable deviation even for slow-diffusing specimen. A drift across the chamber is easily detectable in the concentration image. Thermophoresis of the temperature dye and temperature dependence of the DNA stain are negligible. Our protocols correct for bleaching of fluorescence dyes and inhomogeneous fluorescence illumination.

5.2 Measuring thermophoresis of DNA (Fig. 8)

After checking for possible artefacts, we can now proceed to the experiment. We image the temperature of the infrared-heated water with the fluorescent dye TAMRA in the red-color channel. After bleaching and correcting for inhomogeneous illumination, we extract the temperature image given in Figure 8a. The center of the chamber reveals an increase of temperature by a cross-chamber average of 1.25 K above room temperature. In the green-color channel, we image λ-DNA with the dye SYBR-Green, prepared as described in the methods section. We take the cold image, heat for 300 s without illumination and take a hot image. After correcting for bleaching and the temperature sensitivity of SYBR-Green, we can extract the relative concentration image of DNA (Fig. 8b). DNA is depleted to a cross-chamber average of 60% at the center. Note that the grainy image is not noise, but already the fingerprint of highly diluted single λ-DNA molecules. We do radial averaging of both images (Fig. 8c). This is especially necessary for the noisy temperature image. We fit the radial concentration profile (circles) with the theoretical concentration profile (solid line). The theoretical expectation is inferred from the measured temperature profile with equation (10). We find a nearly perfect fit between measured and calculated concentration profiles for a Soret coefficient $S_T = 0.4\,\mathrm{K}^{-1}$. A full numerical correction of the parabolic z-profile in the chamber changes the result only within experimental noise.

We could infer the diffusion constant of λ-DNA by following the backdiffusion. However, this measurement is quite noisy since the slow diffusion leads to considerable bleaching of SYBR. In future measurements this will be better optimized as we will change to a geometry that is more easily accessible by theory. We will then take images at specific times of the initial depletion to also infer the diffusion constant. Here, we confirmed qualitatively that diffusion is similar to the value of about $D = 1 \times 10^{-12}\,\mathrm{m^2\,s^{-1}}$ published for λ-DNA [22] and rely on the fact that diffusion of molecules is not changed much near a surface [23]. We therefore obtain a thermal diffusion coefficient $D_T = 0.4 \times 10^{-12}\,\mathrm{m^2\,K^{-1}\,s^{-1}}$. We repeat the experiment, adding $500\,\mathrm{mM}$ of NaCl. No thermophoretic depletion can be seen (Fig. 8c, triangles). This indicates that DNA probably follows a similar salt dependence as reported for SDS-micelles [15].
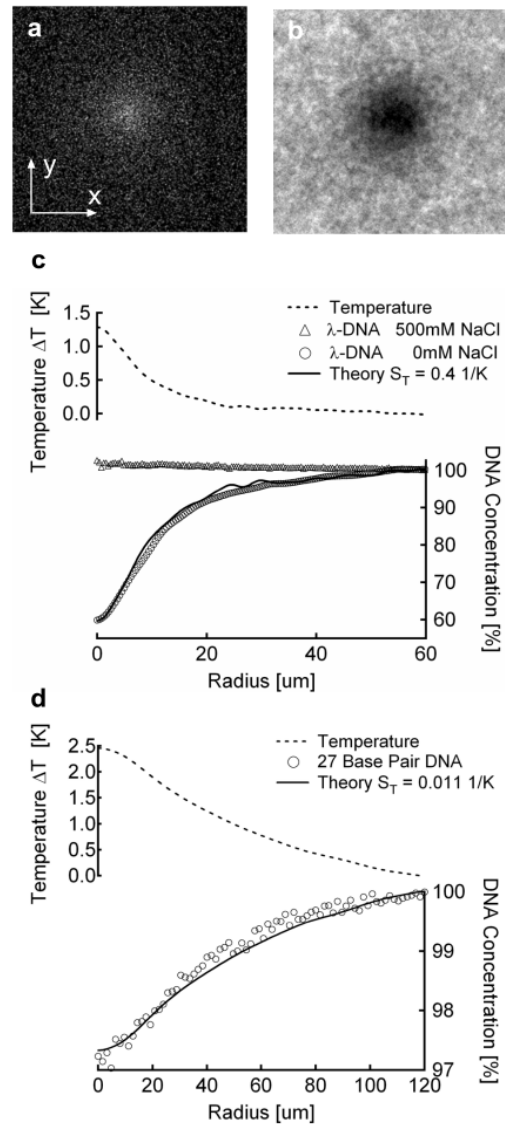

Fig. 8. All-optical thermophoresis measurement of λ-DNA. (a) We image the temperature of the infrared-heated water with the fluorescent dye TAMRA in the red-color channel. After bleaching and illumination correction, we can extract a temperature image. We find the center of the chamber to be heated by 1.25 K above room temperature. (b) In the green-color channel, we image λ-DNA with the dye SYBR-Green I. After bleaching correction and correction for the temperature sensitivity of SYBR, we compute the relative concentration image of DNA. It is depleted to 60% in the heated center. Note that the grainy image is no noise, but the fingerprint of single λ-DNA molecules. (c) Quantitative evaluation is done by radial averaging of above images. Fitting the radial concentration profile with equation (10), using the temperature from the radially averaged temperature image, we find a very good match. The only fitting parameter is the Soret coefficient $S_T = 0.4\,\mathrm{K}^{-1}$. If we add $500\,\mathrm{mM}$ of NaCl, no thermophoretic depletion can be seen. We wait 300 s for the equilibration. Evaluation with full correction of the z-profile in the chamber changes the result only within the noise of the experiment. (d) Also short DNA of 27 base pairs can be measured. The depletion is much less pronounced: we find a Soret coefficient $S_T = 0.011\,\mathrm{K}^{-1}$.

The method is not restricted to large molecules. In Figure 8d, we measured the thermophoresis of a 27 base pair DNA. As expected, the depletion is significantly smaller. The DNA concentration in the center drops only by 2%. The numerical fit (Fig. 8d, solid line) yields a Soret coefficient $S_T = 0.011\,\mathrm{K^{-1}}$. Together with the literature value for the diffusion of DNA of this size [22] of $D = 36 \times 10^{-12}\,\mathrm{m^2\,s^{-1}}$, we can infer a thermal diffusion coefficient $D_T = 0.4 \times 10^{-12}\,\mathrm{m^2\,K^{-1}\,s^{-1}}$. Note that we broadened the heating profile by defocussing the heating laser spot. In this way, we obtain better statistics in the central pixels of the depletion.

5.3 Estimation of error

We give a short overview over the possible error influences discussed beforehand. First of all, the CCD Camera is working at the photon shot noise limit and records intensities with a typical error of 0.5% per pixel. Radial averaging reduces this error greatly down to about 0.05%. This translates to concentration measurement precision of 0.05% and a temperature error of about 0.05 K. This means that Soret coefficients S_T have statistical errors ranging from 2% for large molecules up to 5% for small molecules. As discussed, S_T might be systematically too low by up to 8% as we neglected the thermophoresis of the temperature dye itself. Also, quadratic corrections in the temperature correction of the concentration fluorescence signal can introduce systematic errors of about 1.2%. So far, the method relies on lieterature values for the diffusion coefficient D, which introduces systematical errors of perhaps 30–40%. Small changes in the chamber thickness are not expected to influence the measurement. Therefore, we expect for the method as presented here a precision of about 40% for our measurements. Most of the above error sources will be further optimized in the future. Nevertheless, we accept the above drawbacks since the fluorescence approach gives direct microscopic control over thermophoresis measurements. First of all, fluorescence detection is highly sensitive and allows to measure very low concentrations, down to detecting single molecules. Moreover, we can do thermophoretic measurements in tiny volumes of about $20 \times 20 \times 10\,\mu\mathrm{m}$ (4 femtoliters), opening thermophoretic approaches for highly precious samples. Additionally, the method is selective and only measures thermal diffusion coefficients of the stained molecule even in very complex mixtures. Last but not least, the imaging allows for easy detection of preparation artefacts such as inhomogenous samples, dirt, liquid drift or convection.

5.4 Thermophoresis of DNA under liquid flow (Fig. 9)

We have observed in simulations (Figs. 5 and 7) that thermophoretic depletion can lead to accumulation when the liquid flow works in the opposing direction. Here we show two cases. In both, heating generates a counteracting flow simply by convection. Therefore, only local heating can
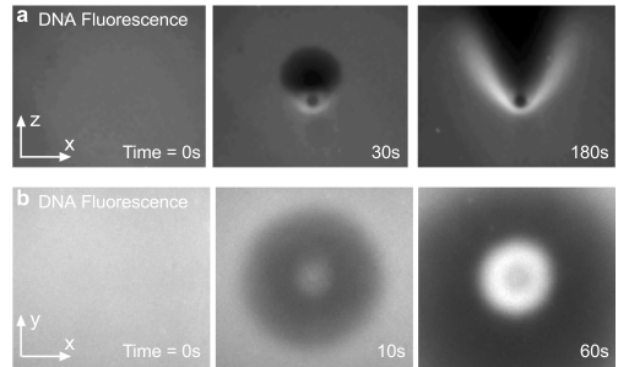

Fig. 9. Accumulation from thermophoresis working against convection. We have seen in simulations (Figs. 5 and 7) that thermophoretic depletion leads to accumulation when the liquid flow works in the opposing direction. We show two cases, where heating generates this flow by convection. Both cases show how convection geometries interact with the thermophoretic drift generated from the same heat source. (a) A vertically oriented glass chamber ($80\,\mu\mathrm{m}$ thick, $500\,\mu\mathrm{m}$ image width) generates a convection pattern in the shape of "∞". At the heating spot, fluid therefore flows from below, slightly from the left and the right side. Since thermophoresis of DNA is opposed, we find a V-shaped pattern, reminiscent of the drift simulation of Figure 7 where the liquid flow is only directed upwards. (b) A similar situation was discussed in detail in equation (6). In a geometry similar to the simulation of Figure 5, a rather thick chamber ($50\,\mu\mathrm{m}$) is heated from below. Thermophoresis and convection lead to a ring-shaped accumulation of DNA near the bottom chamber wall.

lead to accumulation of DNA. It opens to interesting dynamics as convection interacts with thermophoretic drift that is generated from the identical heat source.

In Figure 9a, we see a vertically oriented glass chamber of $80\,\mu\mathrm{m}$ thickness that generates a convection pattern in the shape of "∞". At the heating spot, fluid flows from below, slightly from the left and the right side. Since thermophoresis of DNA is opposing the convection, we find a V-shaped pattern, reminiscent of the drift simulation of Figure 7 where the liquid flow is only directed upwards.

In a second case (Fig. 9b), discussed in more detail in [6], a geometry is studied that is similar to the simulation in Figure 5. A rather thick chamber ($50\,\mu\mathrm{m}$) is heated from below. Thermophoresis and convection leads to a ring-shaped accumulation of DNA near the bottom chamber wall. Both examples show that DNA accumulates in conditions where thermophoretic drift opposes convection flow.

6 Conclusions

We discussed how microfluidic fluorescence under infrared heating can be used to infer thermophoretic constants all-optically. The microscopic setting gives fast equilibration times. The thin chamber efficiently quenches convection below detectable limits. Fluorescence gives optical

resolution ($< 1\,\mu$m) and allows to reach single-molecule sensitivity. Moreover, we can measure thermophoresis of selected molecules in complex and viscous fluid mixtures. Thermophoresis is traditionally used to measure diffusion of molecules [21], an approach which will be accessible also to the femtoliter-sized microfluidic volumes used in this study. Since fluorescence and infrared heating can be performed by a laser scanner in complicated microfluidic designs, the method presented here is able to apply thermophoretic effects in a wide range of interesting settings. The approach will be useful for basic research questions such as single-particle tracking under thermophoresis to resolve the underlying microscopic dynamics of thermophoresis. Moreover, it allows to study thermophoresis near surfaces. With the shown methods, thermophoresis can be applied to various microfluidic applications, such as sorting molecule mixtures by size. In this way, thermophoresis could be an important new biocompatible driving force in microfluidic technologies.

References

1. C. Ludwig, Sitzungsber. Akad. Wiss. Wien, Math.-Naturwiss. Kl. **20**, 539 (1856).
2. C. Soret, Arch. Sci. Phys. Nat. Genève **3**, 48 (1879).
3. J.C. Maxwell, J.C. Collected Papers II, 681-712 (1879) (Cambridge University Press, 1890).
4. P.S. Epstein, Z. Phys. **54**, 537 (1929).
5. S.R. de Groot, P. Mazur, *Non-Equilibrium Thermodynamics* (North-Holland, Amsterdam, 1969).
6. D. Braun, A. Libchaber, Phys. Rev. Lett. **89**, 188103 (2002).
7. K. Clusius, G. Dickel, Z. Phys. Chem. B **44**, 397, (1939).
8. K. Clusius, M. Huber, Z. Naturforsch. A **10**, 230 (1955).
9. M.E. Schimpf, J.C. Giddings, J. Polym. Sci. B **28**, 2673 (1990).
10. B.K. Gale, K.D. Caldwell, A.B. Frazier, IEEE Trans. Biomed. Eng. **45**, 1459 (1998).
11. T.L. Edwards, B.K. Gale, A.B. Frazier, Anal. Chem. **74**, 1211 (2002).
12. D. Braun, A. Libchaber, Phys. Biol. **1**, 1 (2004).
13. W. Köhler, P. Rossmanith, J. Phys. Chem. **99**, 5838 (1995).
14. C. Debuschewitz, W. Köhler, Phys. Rev. Lett. **87**, 055901 (2001).
15. R. Piazza, A. Guarino, Phys. Rev. Lett. **88**, 208302 (2002).
16. S. Iacopini, R. Piazza, Europhys. Lett. **63**, 247253 (2003).
17. R. Rusconi, L. Isa, R. Piazza, J. Opt. Soc. Am. B **21**, 605 (2004).
18. T. Thorsen, S.J. Maerkl, R. Quake, Science **298**, 580 (2002).
19. A. Pluen, P.A. Netti, R.K. Jain, D.A. Berk, Biophys. J. **77**, 542552 (1999).
20. P. Matura, D. Jung, M. Lücke, Phys. Rev. Lett. **92**, 254501 (2004).
21. M. Giglio, A. Vendramini, Phys. Rev. Lett. **38**, 26 (1977).
22. A. Pluen, P.A. Netti, R.K. Jain, D.A. Berk, Biophys. J. **77**, 542 (1999).
23. A. Pralle, E.-L. Florin, E.H.K. Stelzer, J.K.H. Hörber, Appl. Phys. A **66**, S71-S73 (1998).